International Journal of Minerals, Metallurgy and Materials
Volume 26, Number 4, April 2019, Page 404
https://doi.org/10.1007/s12613-019-1749-1

Experimental study on dynamic mechanical property of cemented tailings backfill under SHPB impact loading

Yu-ye Tan[1,2], *Xin Yu*[1,2], *Davide Elmo*[3], *Lin-hui Xu*[1,2], *and Wei-dong Song*[1,2]

1) Key Laboratory of High-Efficient Mining and Safety of Metal Mines (Ministry of Education of China), University of Science and Technology Beijing, Beijing 100083, China

2) School of Civil and Resources Engineering, University of Science and Technology Beijing, Beijing 100083, China

3) Norman B. Keevil Institute of Mining Engineering, Applied Science School, University of British Columbia, Vancouver V6T 1Z4, BC Canada

(Received: 2 November 2018; revised: 11 January 2019; accepted: 22 January 2019)

Abstract: Cemented tailings backfill (CTB) have increasingly been used in recent years to improve the stability of mining stopes in deep underground mines. Deep mining processes are often associated with rock bursting and high-speed dynamic loading conditions. Therefore, it is important to investigate the characteristics and dynamic mechanical behavior of CTB. This paper presents the results of dynamic tests on CTB specimens with different cement and solid contents using a split Hopkinson pressure bar (SHPB). The results showed that some CTB specimens exhibited one to two lower stress peaks after reaching dynamic peak stress before they completely failed. The greater the cement-to-tailings ratio is, the more obvious the strain reaction. This property mainly manifested as follows. First, the dynamic peak stress increased with the increase of the cement-to-tailings ratio when the impact velocity was fixed. Second, the dynamic peak stress had a quadratic relationship with the average stress rate. Third, the cement-to-tailings ratio could enhance the increase rate of dynamic peak stress with strain rate. In addition, the dynamic strength enhancement factor K increased with the increase of strain rate, and its value was larger than that of the rock samples. The failure modes of CTB specimens under low-speed impact were tensile failure and X conjugate shear failure, where were nearly the same as those under static uniaxial and triaxial compression. The CTB specimens were crushed and broken under critical strain, a failure mode similar to that of low-strength concrete. The results of the experimental research can improve the understanding of the dynamic mechanical properties of CTB and guide the strength design of deep mining backfills.

Keywords: impact loading test; cemented tailings backfill; dynamic mechanical properties; split Hopkinson pressure bar

1. Introduction

As surface deposits deplete, mining companies are responding by mining deeper as the demand for mineral resources continues to increase [1]. However, deep mining generates a complex rock mass response including rock bursts that cannot be easily treated using conventional methods [2–4]. At the same time, there is the need to consider the high mining costs and the risks associated with the deposition of large amounts of mine waste into tailings dams or waste dumps, which negatively impacts the surface ground water and the ecological environment [5–8].

In recent years, a newly developed cemented backfilling technology known as cemented tailings backfilling has been increasingly used in deep mining to address the problems above. Cemented tailings backfill (CTB) is an engineered mixture of tailings, binder agents, and water [9–12]. Filling the mined-out area with CTB can greatly help control strata movement and surface subsidence, reduce the amount of waste rocks and tailings, and improve the safety of the working environment [13–15]. In this context, the use of CTB has several advantages compared to conventional backfill methods [16–18] (e.g., rock filling and hydraulic filling).

The knowledge of the mechanical properties of the fill material is a key factor for ensuring the stability of open-

Corresponding author: Davide Elmo E-mail: delmo@mail.ubc.ca

ings and the safety of operators and equipment in adjacent stopes [19]. Many researchers have successfully conducted experimental studies on the static mechanical properties of CTB [20–26]. Some researchers [27–32] determined the internal relationships of deformation characteristics, failure modes, and energy dissipation of CTB at different loading stages and confining pressures. Other researchers [33–35] assessed the effect of curing stress conditions on the mechanical strength and microstructural properties of cemented paste backfills. Dong *et al.* [36] proposed cementitious diagenesis microcosmic rules and explained the hydration mechanism of ultrafine tailings materials under different conditions using X-ray diffraction energy spectrum analysis and scanning electron microscopy. Other previous studies have also shown that backfill components of tailings, binder, and particle size distribution can affect the mechanical and durability properties of CTB [37–38].

Mining processes can result in both static loading and high-velocity (dynamic) impact loading (e.g., blasting and rock burst). These phenomena often cause fracture propagation and damage to backfill bodies, and they may lead to stope collapse. Researchers have explored the stability and mechanical properties of CTB under dynamic loading conditions. Liu and Li [39] conducted dynamic and static strength tests and found that CTB strength increased with loading rate, but only for low strain rate. Li *et al.* [40] analyzed the influence of dynamic loading of a moderate blasting event on CTB stability using LS-DYNA. Zhang *et al.* [41] performed an experiment on high-density tailings backfill (HTB) by subjecting samples to impacts at different velocities using a split Hopkinson pressure bar (SHPB), and they concluded that HTB is likely to be unstable with the increase in strain rate. Moreover, it has been widely acknowledged that the strength of CTB under dynamic loading is significantly higher than that under static loading [41–43].

However, in addition to the three key backfill components (tailings, binder, and particles) size distribution, other factors such as laboratory equipment, strain rate, internal structure, and aggregate composition can affect the strength and the mechanical property of CTB under dynamic loading, and thus, they should be properly considered. This paper fills a gap in the current knowledge of CTB by presenting the results of the sensitivity analysis to better understand the mechanical behavior of CTB. Using an SHPB testing approach, our study focused on the stress–strain response and failure mechanisms of CTB under dynamic loading. The results presented in this paper can improve the current knowledge of the mechanical properties of CTB materials.

2. Experimental

2.1. Materials of CTB specimens

The CTB specimens comprised coarse tailings, binder, and water. The tailings used in the research were collected from a gold mine located in Shandong Province, northeast of China.

2.1.1. Tailings

Tailings were collected from the thickener underflow of the ore processing plant. To obtain a representative and complete range of particle sizes, the tailings samples were collected four times at 10:00 a.m., 12:00 a.m., 14:00 p.m., and 16:00 p.m. for five consecutive days. The damp tailings were first dried in the sun and then in a drying machine under a temperature of 60°C for 12 h.

The particle size distribution of tailings was determined using an LS-C (II A) laser particle size analyzer under dry conditions in accordance with the ASTM D421 standard procedures. Fig. 1 shows the particle size distribution curves of the tested tailings samples. Approximately 10vol% of the fine particles were smaller than 12.13 μm, and the average particle size was 144.26 μm.

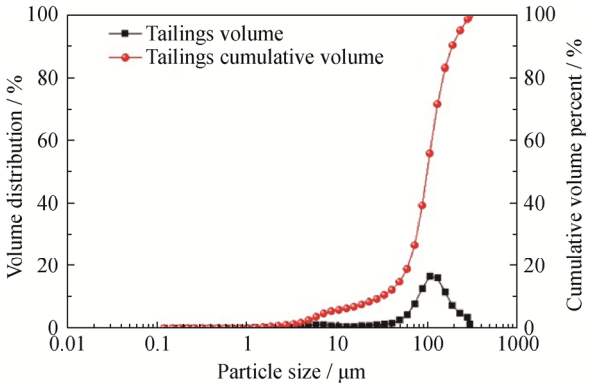

Fig. 1. Particle size distribution of tailings.

The chemical composition of the tailings was obtained using X-ray diffraction (XRD, D8 Advance diffractometer). As shown in Table 1, the SiO_2 content was 65.70wt%. This is not conducive to the performance of binders and is expected to have a slightly negative influence on the strength of the CTB specimens.

Table 1. Main chemical composition of the tailings wt%

SiO_2	Al_2O_3	CaO	MgO	P	Fe	S	Au
65.70	14.3	1.88	0.49	0.08	3.05	0.13	≤ 0.01

2.1.2. Binder and water

Portland cement PC 32.5R was used as binding agent (Table 2). The PC 32.5R is produced in China and is widely used in the mining industry as the basic binding agent in CTB [6]. It contains abundant SiO_2 (21.56wt%) and CaO (62.19wt%), which can provide sufficient strength and stability. Un-distilled water was used to mix tailings and binder and produce slurry. It is important to note that water strongly impacts the mechanical strength property of CTB specimens in terms of the water-to-binder ratio and water content.

Table 2. Chemical composition of Portland cement PC 32.5R wt%

CaO	Al_2O_3	SiO_2	Fe_2O_3	MgO	SiO_3	Na_2O	K_2O	TiO_2
62.19	4.67	21.56	3.69	2.87	1.91	0.21	0.68	0.16

2.2. Size and preparation of CTB specimens

Cement tailings backfill is a type of elastic brittle material equivalent to concrete specimens. The results of existing experimental studies on concrete specimens with different diameters and diameter-to-height ratios have shown that the strength of specimens decreases as their size increases. The International Society of Rock Mechanics and other studies recommend that a cylindrical specimen with a diameter of at least 50 mm should be used for CTB testing [44]. Moreover, Xu *et al.* [45] proposed that the ideal diameter-to-height ratio of cylindrical samples should be between 0.4 and 0.6. In this study, the CTB specimens were designed to be cylindrical with a diameter of 50 mm and diameter-to-height ratio of 0.5–0.6 to satisfy the constraints imposed by the SHPB testing device.

The cement-to-tailings mass ratios used in the experiments were 1:4, 1:6, and 1:8, while the solid content varied between 70wt% and 75wt%. The specimens were cured for 90 d using a standard curing box (Fig. 2). Overall, 30 CTB specimens were tested, including six groups with different cement-to-tailings ratios—Group 70-4-90, Group 75-4-90, Group 70-6-90, Group 75-6-90, Group 70-8-90, and Group 75-8-90—whereby each group had five specimens. The group number represents the corresponding parameters of CTB specimens. For example, Group 70-4-90 means the solid content is 70wt%, the cement-to-tailings ratio is 1:4, and the curing time is 90 d.

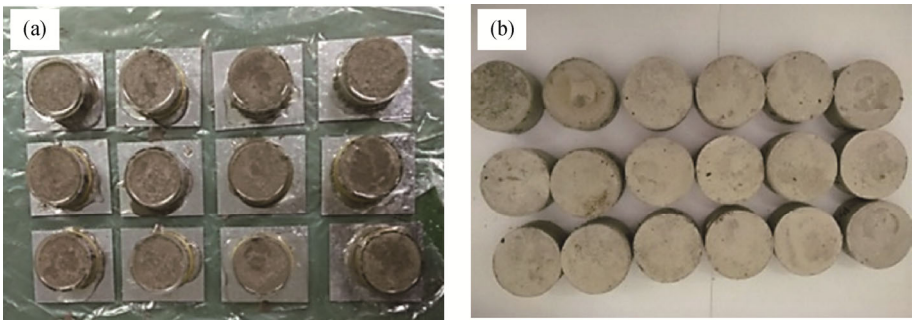

Fig. 2. CTB specimens (a) during and (b) after preparation.

The physical properties of all CTB specimens were measured, and the average values of the physical parameters of each CTB specimen group are shown in Table 3. The quality parameters (quality and density) and the dimension parameters (height, volume, sectional area, and slenderness ratio) of each group were both verified relative to their cement-to-tailings ratios and solid content.

2.3. Split Hopkinson pressure bar

The SHPB (Fig. 3) is considered as an efficient equipment for testing the mechanical response of composite materials, such as rocks and concrete, with high strain rate [45]. During the test, a bullet hits the incident bar at a certain speed and produces a stress wave. The stress wave spreads, first along the incident bar and then across to the interface between the specimen and the elastic rod. Subsequently, part of the stress wave reflects back to the incident bar, while the remainder penetrates into the transmission bar and finally into the absorbing bar.

Assuming that the incident wave propagates into the incident bar with a wave velocity of C_0, the equations for the strain rate $\frac{\mathrm{d}\varepsilon_s}{\mathrm{d}t}$, strain ε_s, and stress σ_s can be determined as follows [44]:

$$\frac{\mathrm{d}\varepsilon_s}{\mathrm{d}t}=\frac{C_0}{l_0}(\varepsilon_i-\varepsilon_r-\varepsilon_t) \tag{1}$$

$$\sigma_s=\frac{EA}{2A_0}(\varepsilon_i+\varepsilon_r+\varepsilon_t) \tag{2}$$

$$\varepsilon_s=\frac{C_0}{l_0}\int_0^t(\varepsilon_i-\varepsilon_r-\varepsilon_t)\mathrm{d}t \tag{3}$$

Table 3. Physical parameters of CTB specimens (ϕ50 mm)

Group	Number	Mass / kg	Density / (kg·m^{-3})	Height / mm	Volume / cm^3	Sectional area / cm^2	Slenderness ratio
	1	0.094	1732.05	27.64	54.27	19.63	0.55
	2	0.091	1768.93	26.20	51.44	19.63	0.52
70-4-90	3	0.101	1842.37	27.92	54.82	19.63	0.56
	4	0.103	1780.63	29.46	57.84	19.63	0.59
	5	0.108	1833.46	30.00	58.90	19.63	0.60
	1	0.102	1774.19	29.28	57.49	19.63	0.59
	2	0.107	1775.07	30.70	60.28	19.63	0.61
75-4-90	3	0.102	1825.30	28.46	55.88	19.63	0.57
	4	0.099	1771.62	28.46	55.88	19.63	0.57
	5	0.099	1765.42	28.56	56.08	19.63	0.57
	1	0.102	1747.92	29.72	58.36	19.63	0.59
	2	0.099	1725.54	29.22	57.37	19.63	0.58
70-6-90	3	0.089	1665.22	27.22	53.45	19.63	0.54
	4	0.095	1675.32	28.88	56.71	19.63	0.58
	5	0.096	1779.20	27.48	53.96	19.63	0.55
	1	0.096	1787.00	27.36	53.72	19.63	0.55
	2	0.104	1748.08	30.30	59.49	19.63	0.61
75-6-90	3	0.101	1752.01	29.36	57.65	19.63	0.59
	4	0.102	1803.76	28.80	56.55	19.63	0.58
	5	0.093	1691.59	28.00	54.98	19.63	0.56
	1	0.098	1688.46	29.56	58.04	19.63	0.59
	2	0.087	1582.45	28.00	54.98	19.63	0.56
70-8-90	3	0.097	1792.51	27.56	54.11	19.63	0.55
	4	0.089	1672.60	27.10	53.21	19.63	0.54
	5	0.096	1701.20	28.74	56.43	19.63	0.57
	1	0.096	1673.25	29.22	57.37	19.63	0.58
	2	0.095	1690.53	28.62	56.20	19.63	0.57
75-8-90	3	0.092	1713.80	27.34	53.68	19.63	0.55
	4	0.095	1652.43	29.28	57.49	19.63	0.59
	5	0.105	1806.62	29.60	58.12	19.63	0.59

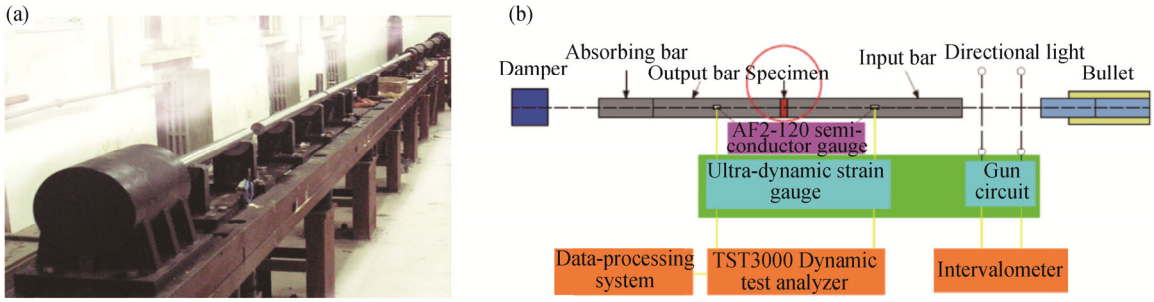

Fig. 3. Physical map (a) and schematic diagram (b) of split Hopkinson pressure bar testing system.

where E is the elastic modulus of the press bar (MPa); A and A_0 are the cross-sectional areas of the press bar and the specimen, respectively (m^2); l_0 is the height of the sample (mm); and ε_i, ε_r, and ε_t are the input, reflection, and

transmission signals, respectively.

3. Results and discussion

3.1. Dynamic mechanical test

SHPB impact loading tests were performed on Group 70-4-90 to derive the impact waveform diagram of the CTB specimens (Fig. 4). The voltage peaks of the incident and transmission waves increased with increasing impact rate. The amplitudes of the incident and reflected waves manifested the same tendencies, but their values were greater than that of the reflected wave. This phenomenon can be explained by wave impedance theory [46]; that is, the wave impedance between the incident bar and the CTB specimen was large. The stress amplitude of the transmission wave was much smaller than that of the incident waves. This means energy decreased rapidly when going through the CTB specimens. This is a good indicator that the CTB specimen exhibits strong damping and shielding effect with respect to propagation of the elastic wave, which will be beneficial to the stability of CTB materials in an underground mining stope.

According to previous research results [38–43], impact velocities between 2.5 and 7.5 $m \cdot s^{-1}$ can be used for SHPB impact loading tests on CTB specimens. In this experiment, signal values and failure modes were recorded, and the strain rate and peak stress were calculated according to Eqs. (1), (2), and (3).

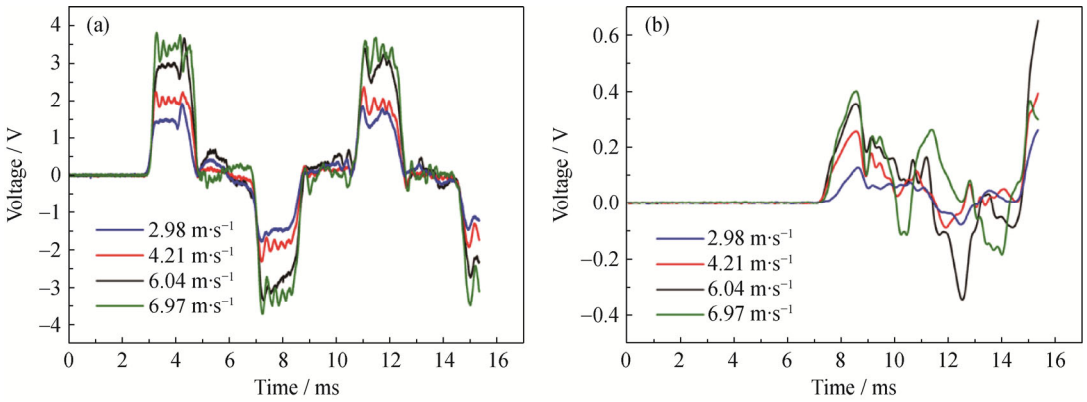

Fig. 4. SHPB impact waveform of Group 70-4-90: (a) incident and reflected wave curves; (b) transmission wave curves.

3.2. Characteristics and relationship of stress and strain

The stress–strain curves of the different CTB specimen groups are shown in Fig. 5. First, when the solid content and the cement-to-tailings ratios were constant, the dynamic peak stress of the CTB specimens increased with the increase of impact velocity. Second, the cement-to-tailings ratios significantly influenced the dynamic peak stress of the CTB specimens. Under a similar impact velocity, the larger the cement-to-tailings ratios, the greater the dynamic peak stresses of the CTB specimens. Third, when the solid content and the cement-to-tailings ratios were constant, with the increase of impact velocity, the strain tended to increase with the dynamic peak stress. However, the strain value under SHPB impact loading tests was much lower than the maximum strain value under static compression, given the same solid content and cement-to-tailings ratios.

The deformation and failure process were analyzed and characterized in terms of four stages (Fig. 6.). The results agree with observations in Refs. [10,27–35,46–47].

(1) Micro-crack closure stage (A). The curve has a concave shape, which indicates that the internal crack gradually closed under compressive pressure and the CTB specimen generated nonlinear deformation. However, in the experiments, this part of the curve was not obvious or difficult to observe (e.g., No. 75-4-90-5).

(2) Elastic deformation stage (B). Stress concentration occurs around the inner primordial pore, but the corresponding value is not sufficiently large to extend and burst the internal micro-cracks. In accordance with Hooke's law, the curve approximates a straight line. The slope of the line is regarded as the elastic modulus of the CTB specimens.

(3) Inelastic stage (C). The curve becomes convex, which suggests that the CTB specimen has started to undergo inelastic deformation. The value of the stress around the micro-crack exceeds the limit, which results in inner-crack expansion and rupture. The original damage gradually propagates and worsens until the stress reaches the peak at point C.

(4) Crack penetration and failure stage (D). The micro-cracks continue to expand and bifurcate. Then, the

deformation of the CTB specimens begins to weaken. Leading cracks gradually form parallel to the principal stress direction, and the CTB specimens crack and eventually become fully damaged.

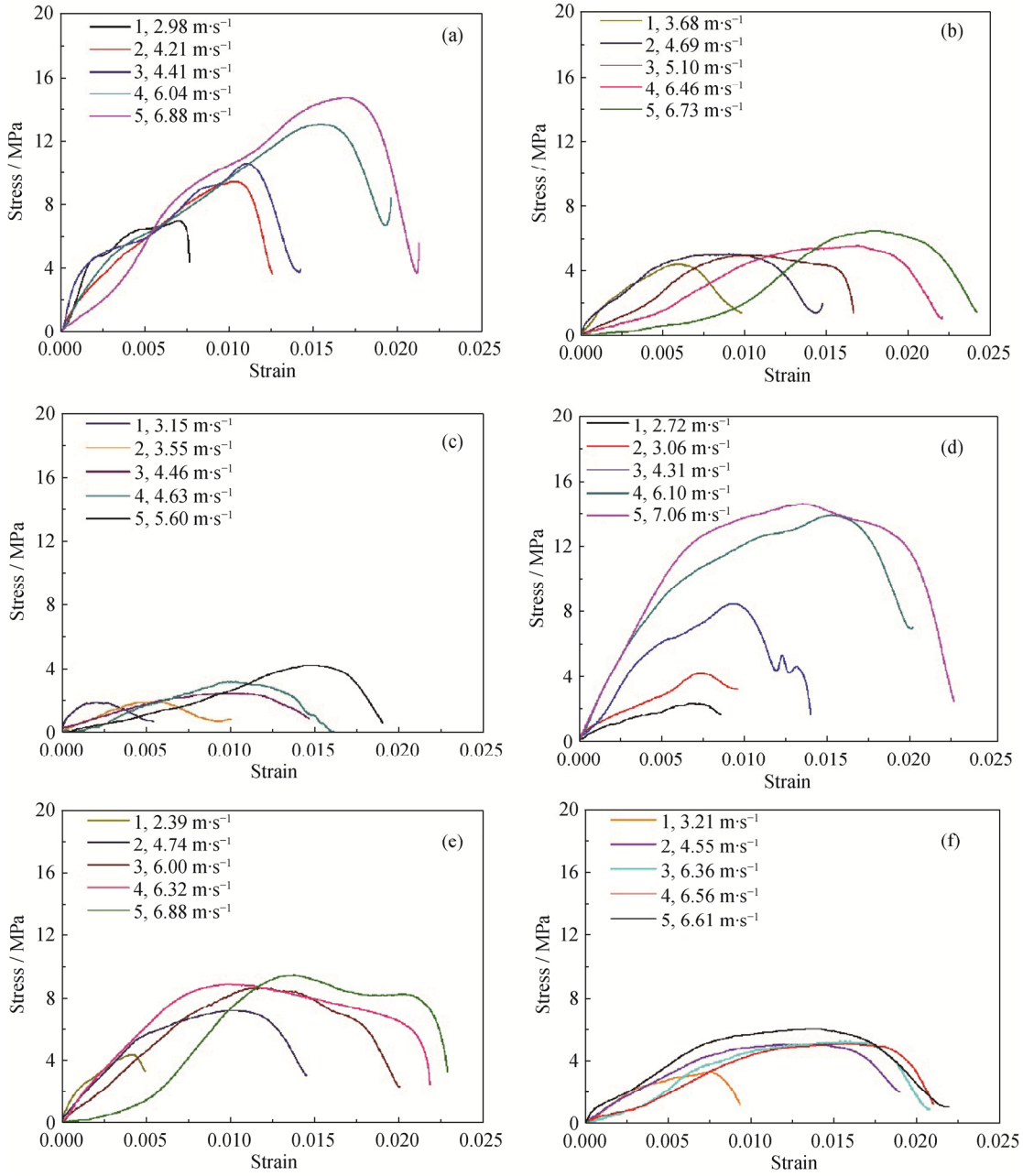

Fig. 5. Stress–strain curves of CTB specimens during the impact loading test by SHPB: (a) Group 70-4-90; (b) Group 70-6-90; (c) Group 70-8-90; (d) Group 75-4-90; (e) Group75-6-90; (f) Group 75-8-90.

Some CTB specimens did not completely break, but their stress waves dropped to one to two lower stress peaks after dynamic peak stress (Fig. 7). This specific finding differs from that of stress–strain curves of general brittle rocks under dynamic loading or CTB specimens under static loading [47], which do not rebound after dynamic peak stress. In this situation, the stress started to decrease because only parts of the CTB specimens were damaged after the dynamic peak stress. Then, the stress gradually increased to a second lower stress peak, and the micro-cracks in the undamaged parts started to become compressed and compacted. This phenomenon appeared once or twice until the CTB specimens became completely destroyed.

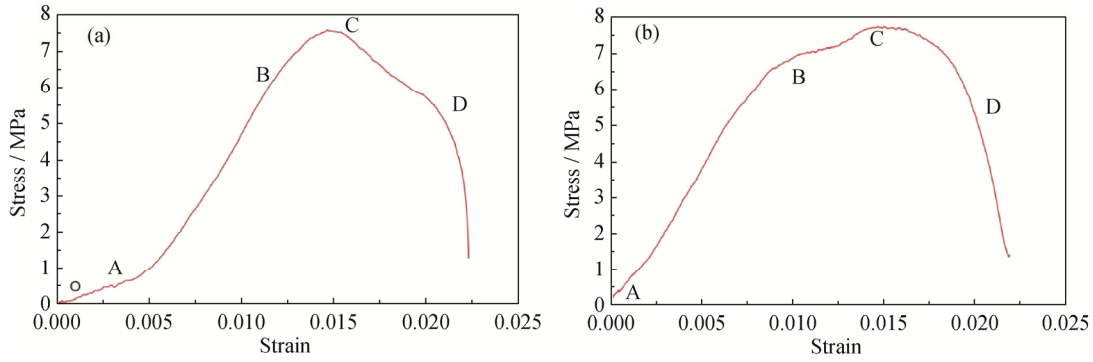

Fig. 6. Deformation stages of CTB specimens under SHPB impact loading tests: (a) No. 75-4-90-4; (b) No. 75-4-90-5.

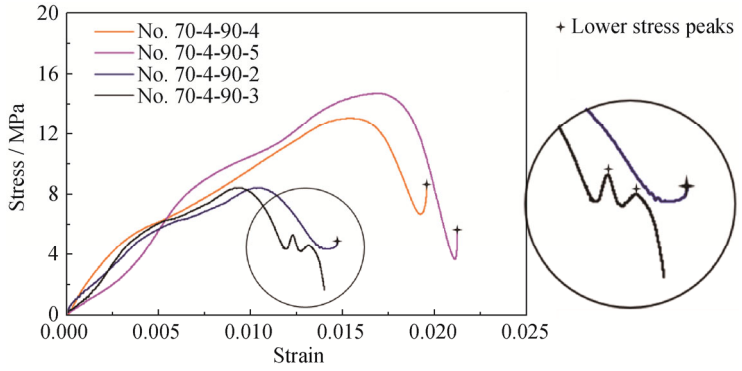

Fig. 7. Stress–strain curves of CTB specimens showing the stress dropping to one to two lower stress peaks after the dynamic peak stress.

3.3. Dynamic strength characteristic

The complete results are shown in Table 4, in which the dynamic strength enhancement factor K denotes the increase of dynamic peak stress (σ_p) relative to static compressive strength (σ) [46], which can be calculated with the following equation:

$$K = \frac{\sigma_p}{\sigma} \tag{4}$$

The strain rate of the CTB specimens gradually increased with the increase of impact velocity, and the increase is larger than the one generally observed in the rock samples [47]. Additionally, the dynamic peak strength of the CTB specimens increased with the increase of strain rate. For example, the average stress rate of Group 70-4-9 increased from 29 to 91 s^{-1}, which subsequently cause the dynamic peak stress to increase from 7.00 to 14.74 MPa. According to the regression analysis (Table 5), the relationship between dynamic peak stress σ_P and average stress rate ε represents an exponential best fitting, as shown in Fig. 8. Generally, the higher the cement-to-tailings ratios, the faster the increase of the dynamic peak stress with average stress rate. But Group 75-6-90 presented a curve (Fig. 8(b)) with a slightly decreasing trend when the average stress rate was around 80 s^{-1}.

Moreover, when the average stress rate was between 30 and 40 s^{-1}, the value of dynamic peak stress of the CTB specimens approximated that of static compressive strength, and the factor K values were nearly 1. However, factor K increased with the increase of stress rate. As a result, when the stress rate was between 80 and 100 s^{-1}, the dynamic peak stresses were two to three times of those of static compression strength, and even 4.01 times those of some CTB specimens (e.g., No. 70-4-90-5). These values were much higher than those of the rock samples, and the factor K was only 1.20–2.50 [46–47].

Moreover, given a constant solid content, the greater the cement-to-tailings ratio, the higher the K. Additionally, the greater the cement-to-tailings ratio, the faster the change of the variation rate of the dynamic peak stress with stress rate. These scenarios suggest that the variation efficiency of the strain increases with the increase of cement-to-tailings ratio.

3.4. Dynamic failure characteristic

The CTB specimens were destroyed and broken instantaneously under high-speed SHPB impact loading test. A high-definition camera was used to record the complete impact and failure process (Figs. 9(a) and 9(b)).

Table 4. Experimental result of impact loading test by SHPB

Group	Number	Impact velocity, C / (m·s^{-1})	Max stress rate, ε_s / s^{-1}	Average stress rate, ε / s^{-1}	Dynamic peak stress, σ_P / MPa	K	Static compression strength, σ / MPa
70-4-90	1	2.98	42	29	7.00	1.90	3.68
	2	4.21	80	52	9.39	2.55	
	3	4.41	84	57	10.58	2.88	
	4	6.04	115	81	13.02	3.54	
	5	6.88	128	91	14.74	4.01	
75-4-90	1	2.81	40	26	6.52	1.19	5.48
	2	3.06	58	39	7.17	1.31	
	3	4.31	71	51	8.43	1.54	
	4	6.10	128	84	13.88	2.53	
	5	7.06	135	95	15.91	2.90	
70-6-90	1	3.68	72	44	4.42	2.08	2.13
	2	4.69	89	60	4.82	2.26	
	3	5.10	101	69	5.35	2.51	
	4	6.46	133	93	6.57	3.08	
	5	6.73	135	97	7.47	3.51	
75-6-90	1	2.39	30	20	4.35	1.16	3.74
	2	4.74	90	60	7.87	2.10	
	3	6.00	124	85	8.66	2.32	
	4	6.32	130	90	8.89	2.38	
	5	6.88	131	90	9.44	2.52	
70-8-90	1	3.15	48	30	1.88	1.06	1.78
	2	3.55	53	42	1.93	1.08	
	3	4.46	80	60	2.46	1.38	
	4	4.63	88	64	3.18	1.79	
	5	5.60	115	80	4.24	2.38	
75-8-90	1	3.21	52	39	3.29	1.26	2.61
	2	4.55	115	79	5.04	1.93	
	3	6.36	116	84	5.07	1.94	
	4	6.56	115	86	5.23	2.00	
	5	6.61	132	88	6.05	2.32	

Table 5. Regression analysis results on dynamic peak stress and average stress rate

Group	Polynomial fitting	Linear fitting	Exponential fitting	Power fitting
70-4-90	$\sigma_p = 0.000226\varepsilon^2 + 0.096\varepsilon + 4.048$, $R^2 = 0.986$	$\sigma_p = 0.1230\varepsilon + 3.3233$, $R^2 = 0.991$	$\sigma_p = 871.6 - 868.3e^{-0.00014\varepsilon}$, $R^2 = 0.992$	$\sigma_p = 0.689\varepsilon^{0.674}$, $R^2 = 0.985$
70-6-90	$\sigma_p = 0.000731\varepsilon^2 - 0.0504\varepsilon + 5.236$, $R^2 = 0.949$	$\sigma_p = 0.0549\varepsilon + 1.7393$, $R^2 = 0.940$	$\sigma_p = 3.96 + 0.106e^{0.0355\varepsilon}$, $R^2 = 0.978$	$\sigma_p = 0.300\varepsilon^{0.690}$, $R^2 = 0.926$
70-8-90	$\sigma_p = 0.00106\varepsilon^2 - 0.0689\varepsilon + 2.960$, $R^2 = 0.943$	$\sigma_p = 0.0473\varepsilon + 0.1282$, $R^2 = 0.870$	$\sigma_p = 1.415 + 0.113e^{0.0404\varepsilon}$, $R^2 = 0.964$	$\sigma_p = 0.047\varepsilon^{1.012}$, $R^2 = 0.868$
75-4-90	$\sigma_p = 0.000131\varepsilon^2 - 0.0194\varepsilon + 6.050$, $R^2 = 0.996$	$\sigma_p = 0.142\varepsilon + 1.996$, $R^2 = 0.977$	$\sigma_p = e^{1.557+0.010\varepsilon+0.00003\varepsilon^2}$, $R^2 = 0.997$	$\sigma_p = 0.385\varepsilon^{0.811}$, $R^2 = 0.967$
75-6-90	$\sigma_p = 0.000625\varepsilon^2 + 0.1359\varepsilon + 1.894$, $R^2 = 0.970$	$\sigma_p = 0.066\varepsilon + 3.277$, $R^2 = 0.959$	$\sigma_p = e^{1.030+0.025\varepsilon+0.00013\varepsilon^2}$, $R^2 = 0.982$	$\sigma_p = 1.080\varepsilon^{0.475}$, $R^2 = 0.980$
75-8-90	$\sigma_p = 0.00118\varepsilon^2 - 0.101\varepsilon + 5.431$, $R^2 = 0.862$	$\sigma_p = 0.047\varepsilon + 1.424$, $R^2 = 0.903$	$\sigma_p = e^{1.425-0.014\varepsilon+0.00020\varepsilon^2}$, $R^2 = 0.934$	$\sigma_p = 0.291\varepsilon^{0.657}$, $R^2 = 0.897$

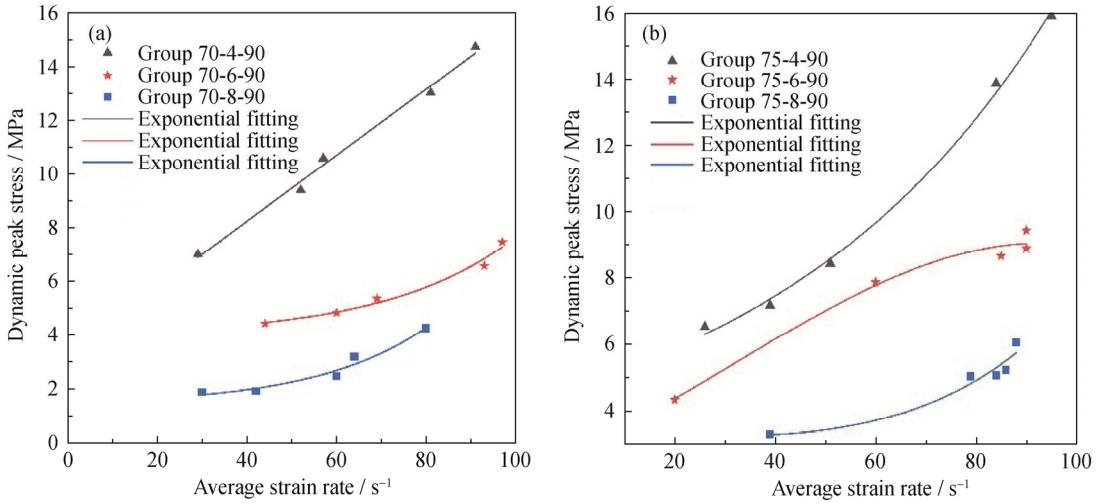

Fig. 8. Relation curves of dynamic peak stress and average stress rate for different solid contents: (a) Group with solid content 70wt%; (b) Group with solid content 75wt%. All curves represent a quadratic relationship.

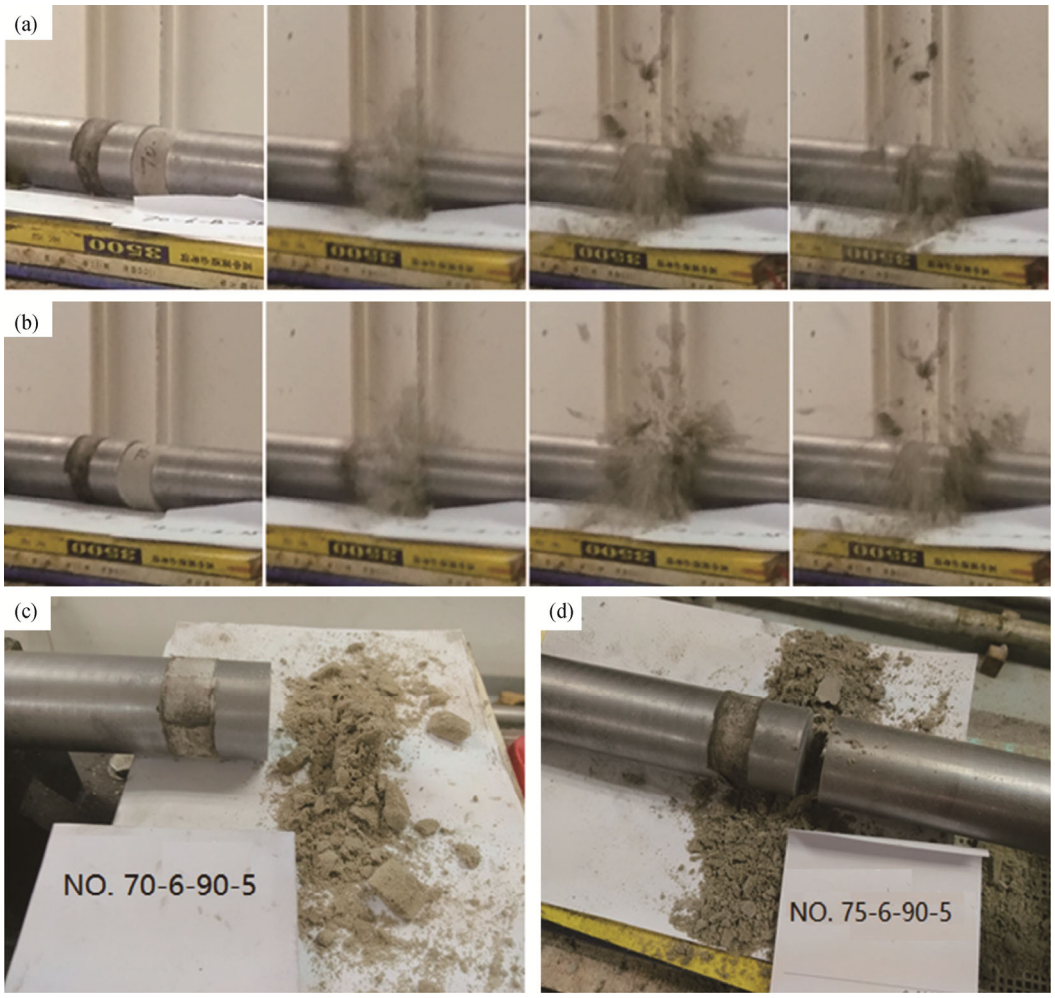

Fig. 9. Failure process of CTB specimens No. 70-6-90-5 (a) and No. 75-6-90-5 (b) under high-velocity impact loading (6.37 m·s^{-1} on No. 70-6-90-5 and 6.88 m·s^{-1} on No. 75-6-90-5) by SHPB and failure results of CTB specimens No. 70-6-90-5 (c) and No. 75-6-90-5 (d).

The failure modes of the CTB specimens under low impact velocity (approximately 4–5 m·s^{-1}) were nearly the same as those of tests performed under uniaxial and triaxial static compression [47]. There were three main types of

failure: tensile failure I (Fig. 10(a)), in which the direction of the fracture surface was consistent with the loading direction; X conjugate shear failure (Fig. 10(b)), which was in first tension along cracks the but final shear failure; and tensile failure II (Fig. 10(c)). Due to the heterogeneity, failure mainly resulted from tensile damage, but shear damage still existed, which also influenced the shear strength.

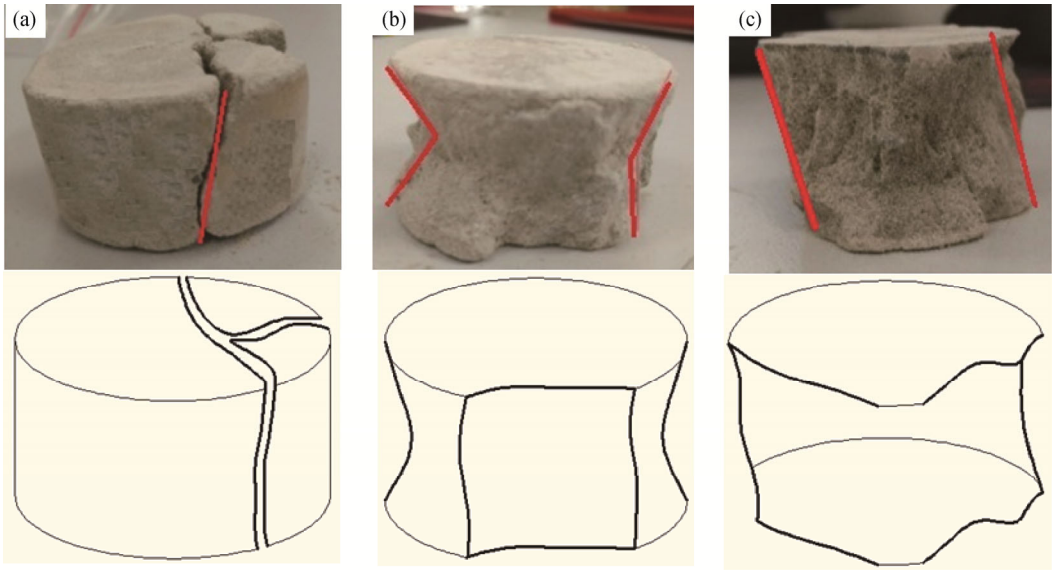

Fig. 10. Failure modes of CTB specimens under low-velocity impact of SHPB. Three main types of failure: (a) tensile failure I for No. 70-6-90-2 and No. 75-4-90-2 under impact velocities of 4.69 m·s^{-1} and 4.31 m·s^{-1}; (b) X conjugate shear failure for No. 75-8-90-2 and No. 75-6-90-2 under impact velocities of 4.55 m·s^{-1} and 4.74 m·s^{-1}; (c) tensile failure II for No. 70-8-90-2 and No. 70-4-90-3 under impact velocities of 4.46 m·s^{-1} and 4.41 m·s^{-1}.

The failure modes and the destruction degree of the CTB specimens changed with the variation of impact velocity. For example, as shown in Fig. 11, the failure modes of five CTB specimens in Group 70-6-90 differed greatly. No. 70-6-90-1 almost had no destruction and remained whole under the low impact velocity of 3.68 m·s^{-1}. No. 70-6-90-2 was remained whole at first, but started to break from the peripheral and exhibited few fine cracks under the impact velocity of 4.69 m·s^{-1}. No. 70-6-90-3 was split into parts along the main cracks, which resulted in perforation failure under the impact velocity 5.10 m·s^{-1}, but was still kept together with minimal residual strength. No. 70-6-90-4 was crushed into several small parts and exhibited complete instability. No. 70-6-90-5 was crushed into small pieces under the high crush power and was completely destroyed. The higher the impact velocity and the stress rate is, the much higher the crushing degree of the CTB specimen. When the average stress rate was less than 50 s^{-1}, only the surrounding area of the sample was broken after being impacted (Figs. 11(a) and 11(b)). When the stress rate increased to approximately 69 s^{-1}, the CTB specimen broke into few parts along the main cracks, and micro-cracks appeared in both the broken and unbroken areas, but the CTB specimen continued to exhibit some residual strength (Fig. 11(c)). When the stress rate increased to approximately 90 s^{-1}, crushing instability occurred (Figs. 11(d) and 11(e)). This phenomenon indicates that the limit instability stress rate of a specimen group is approximately 90 s^{-1}. At the limit stress rate, the CTB specimens exhibited complete crushing failure, which is similar to the failure form of low-strength concrete samples. Under the dynamic impact of SHPB, the CTB specimens cracked rapidly, with ejection fragments, along the radial direction.

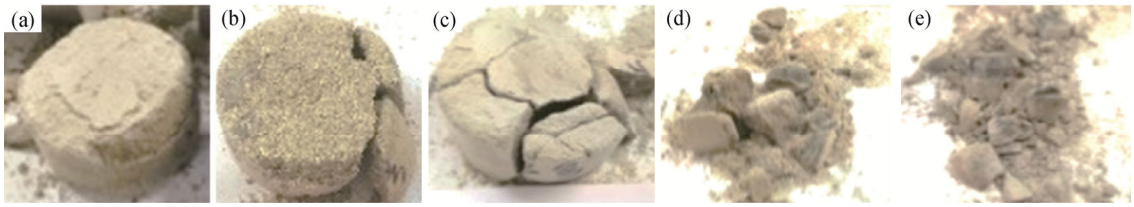

Fig. 11. Failure modes and destruction degree of Group 70-6-90: (a) No. 70-6-90-1; (b) No. 70-6-90-2; (c) No. 70-6-90-3; (d) No. 70-6-90-4; (e) No. 70-6-90-5.

4. Conclusions

In this study, a series of dynamic loading tests on CTB specimens by SHPB was conducted to explore the dynamic mechanical property of CTB. The characteristics and relationship of stress and strain, dynamic strength characteristic, and dynamic failure characteristic were analyzed to obtain some useful conclusions, which are as follows:

(1) The deformation of CTB specimens can be divided into four stages: micro-crack closure stage, elastic deformation stage, inelastic stage, and penetration and failure stage. Some CTB specimens did not break immediately after dynamic peak stress. The micro-cracks in the unbroken areas of the CTB specimens were compressed and became compacted; as a result, the specimens exhibited one to two lower stress peaks before they were completely broken.

(2) The dynamic peak stress of the CTB specimens increased with the increase of impact velocity and was significantly affected by cement-to-tailings ratio. The higher the cement-to-tailings ratio, the greater the dynamic peak stress under a similar impact velocity. The curve of dynamic peak stress and the average stress rate represents a quadratic relationship. Moreover, the higher the cement-to-tailings ratio, the faster the increase of the dynamic peak stress with average stress rate. All these scenarios indicate that variation efficiency became remarkable when the cement-to-tailings ratio of the CTB specimen was high. The finding further indicates that the variation efficiency of the strain increases with the increase of cement-to-tailings ratio.

(3) The value of dynamic peak stress of the CTB specimens under low strain was close to that of static compression strength. With the increase of stress rate, the factor K also increased. The increase could be twice to thrice and even 4.01 times that of static compression strength when the limit stress rate was reached. The values were higher than those of the factor K of the rock samples. When the solid content was constant, the higher the cement-to-tailings ratio is, the greater the factor K.

(4) The failure modes of the CTB specimens under low-speed impact were nearly the same as those under static uniaxial and axial compression and manifested as X conjugate shear failure, tensile failure, and shear failure. However, at the limit stress rate, the CTB specimens were mainly crushed, a failure form similar to that of low-strength concrete samples.

Acknowledgements

This work was financially supported by the National Key R&D Program of China (No. 2018YFC0604602), the Fundamental Research Funds for the Central Universities of China (No. FRF-TP-17-029A2), and the Open fund of Key Laboratory of High-Efficient Mining and Safety of Metal Mines, Ministry of Education of China (No. ustbmslab201803).

References

[1] M.C. He, H.P. Xie, S.P. Peng, and Y.D. Jiang, Study on rock mechanics in deep mining engineering, *Chin. J. Rock Mech. Eng.*, 24(2005), No. 16, p. 2803.

[2] F.P. Hassani, A. Mortazavi, and M. Shabani, An investigation of mechanisms involved in backfill-rock mass behavior in narrow vein mining, *J. South Afr. Inst. Min. Metall.*, 108(2008), No. 8, p. 463.

[3] R. Rankine, M. Pacheco, and N. Sivakugan, Underground mining with backfills, *Soils Rocks*, 30(2007), No. 2, p. 93.

[4] P. Li, M.F. Cai, Q.F. Guo, and S.J. Miao, Characteristics and implications of stress state in a gold mine in Ludong area, China, *Int. J. Miner. Metall. Mater.*, 25(2018), No. 12, p. 1363.

[5] M. Benzaazoua, B. Bussière, I. Demers, M. Aubertin, É. Fried, and A. Blier, Integrated mine tailings management by combining environmental desulphurization and cemented paste backfill: Application to mine Doyon, Quebec, Canada, *Miner. Eng.*, 21(2008), No. 4, p. 330.

[6] M. Fall and M. Pokharel, Coupled effects of sulphate and temperature on the strength development of cemented tailings backfills: Portland cement-paste backfill, *Cem. Concr. Compos.*, 32(2010), No. 10, p. 819.

[7] N. Sivakugan, R.M. Rankine, K.J. Rankine, and K.S. Rankine, Geotechnical considerations in mine backfilling in Australia, *J. Cleaner Prod.*, 14(2006), No. 12-13, p. 1168.

[8] L. Yang, J.P. Qiu, H.Q. Jiang, S.Q. Hu, H. Li, and S.B. Li, Use of cemented super-fine uncoarse tailings backfill for control of subsidence, *Minerals*, 7(2017), No. 11, p. 216.

[9] Z.X. Liu, W.G. Dang, and X.Q. He, Undersea safety mining of the large gold deposit in Xinli District of Sanshandao Gold Mine, *Int. J. Miner. Metall. Mater.*, 19(2012), No. 7, p. 574.

[10] S. Ouellet, B. Bussière, M. Aubertin, and M. Benzaazoua, Microstructural evolution of cemented paste backfill: Mercury intrusion porosimetry test results, *Cem. Concr. Compos.*, 37(2007), No. 12, p. 1654.

[11] E. Yilmaz, T. Belem, and M. Benzaazoua, Specimen size effect on strength behavior of cemented paste backfills subjected to different placement conditions, *Eng. Geol.*,

185(2015), p. 52.

[12] V.F.N. Torres, C.D. da Gama, M.C. e Silva, P.F. Neves, and Q. Xie, Comparative stability analyses of traditional and selective room-and-pillar mining techniques for sub-horizontal tungsten veins, *Int. J. Miner. Metall. Mater.*, 18(2011), No. 1, p. 1.

[13] J.X. Zhang, B.Y. Li, N. Zhou, and Q. Zhang, Application of solid backfilling to reduce hard-roof caving and longwall coal face burst potential, *Int. J. Rock Mech. Min. Sci*., 88(2016), p. 197.

[14] D.Q. Deng, L. Liu, Z.L. Yao, K.I.I.L. Song, and D.Z. Lao, A practice of ultra-fine tailings disposal as filling material in a gold mine, *J. Environ. Manage*., 196(2017), p. 100.

[15] X. Ke, H.B. Hou, M. Zhou, Y. Wang, and X. Zhou, Effect of particle gradation on properties of fresh and hardened cemented paste backfill, *Constr. Build. Mater.*, 96(2015), p. 378.

[16] A. Khoshand and M. Fall, Geotechnical characterization of peat-based landfill cover materials, *J. Rock Mech. Geotech. Eng.*, 8(2016), No. 5, p. 596.

[17] M. Li, J.X. Zhang, N. Zhou, and Y.L. Huang, Effect of particle size on the energy evolution of crushed waste rock in coal mines, *Rock Mech. Rock Eng.*, 50(2017), No. 5, p. 1347.

[18] L. Cui and M. Fall, Mechanical and thermal properties of cemented tailings materials at early ages: Influence of initial temperature, curing stress and drainage conditions, *Constr. Build. Mater.*, 125(2016), p. 553.

[19] B. Ercikdi, A. Kesimal, F. Cihangir, H. Deveci, and İ. Alp, Cemented paste backfill of sulphide-rich tailings: Importance of binder type and dosage, *Cem. Concr. Compos.*, 31(2009), No. 4, p. 268.

[20] C. Liu, B. Han, W. Sun, J.X. Wu, S. Yao, and H.Y. Hu, Experimental study of strength of backfilling of cemented rock debris and its application under low temperature condition, *Chin. J. Rock Mech. Eng.*, 34(2015), No. 1, p. 139.

[21] D.R. Tesarik, J.B. Seymour, and T.R. Yanske, Long-term stability of a backfilled room-and-pillar test section at the Buick Mine, Missouri, USA, *Int. J. Rock Mech. Min. Sci.*, 46(2009), No. 7, p. 1182.

[22] J.S. Chen, B. Zhao, X.M. Wang, Q.L. Zhang, and L. Wang, Cemented backfilling performance of yellow phosphorus slag, *Int. J. Miner. Metall. Mater.*, 17(2010), No. 1, p. 121.

[23] R.J. Marsal, *Mechanical Properties of Rockfill Embankment Dam Engineering*, John Wiley Sons Inc., New York, 1973, p. 109.

[24] M. Fall, M. Benzaazoua, and S. Ouellet, Experimental characterization of the influence of tailings fineness and density on the quality of cemented paste backfill, *Miner. Eng.*, 18(2005), No. 1, p. 41.

[25] A. Kesimal, E. Yilmaz, B. Ercikdi, İ. Alp, M. Yumlu, and B. Ozdemir, Laboratory testing of cemented paste backfill, *Madencilik*, 41(2002), No. 4, p. 11.

[26] G.Y. Zhao, H. Wu, Y. Chen, Z.W. Xu, Z.Y. Li, and E.J. Wang, Experimental study on load-bearing mechanism and compaction characteristics of mine filling materials, *J. China Univ. Min. Technol.*, 46(2017), No. 6, p. 1251.

[27] W.B. Xu, W.D. Song, D.X. Wang, B.G. Yang, and W.D. Pan, Energy dissipation properties of cement backfill body under triaxle compression conditions, *J. China Univ. Min. Technol.*, 43(2014), No. 5, p. 808.

[28] W.B. Xu, P.W. Cao, and M.M. Tian, Strength development and microstructure evolution of cemented tailings backfill containing different binder types and contents, *Minerals*, 8(2018), No. 4, p. 167.

[29] W.B. Xu, X.C. Tian, and P.W. Cao, Assessment of hydration process and mechanical properties of cemented paste backfill by electrical resistivity measurement, *Nondestr. Test. Eval.*, 33(2018), No. 2, p. 198.

[30] W.B. Xu and P.W. Cao, Fracture behaviour of cemented tailing backfill with pre-existing crack and thermal treatment under three-point bending loading: Experimental study and particle flow code simulation, *Eng. Fract. Mech.*, 195(2018), p. 129.

[31] W.B. Xu, X.C. Tian, and C.B. Wan, Prediction of mechanical performance of cemented paste backfill by the electricity resistivity measurement, *J. Test. Eval.*, 46(2018), No. 6, p. 2450.

[32] W.B. Xu, Y.B. Hou, W.D. Song, Y.P. Zhou, and T.J. Yin, Resistivity and thermal infrared precursors associated with cemented backfill mass, *J. Cent. South Univ.*, 23(2016), No. 9, p. 2329.

[33] E. Yilmaz, A. Kesimal, and B. Ercikdi, Evaluation of acid producing sulphidic mine tailings as a paste backfill, *Turk. J. Earth Sci. Rev.*, 17(2004), No. S1, p. 11.

[34] E. Yilmaz, T. Belem, M. Benzaazoua, A. Kesimal, and B. Ercikdi, Evaluation of the strength properties of deslimed tailings paste backfill, *Miner. Resour. Eng.*, 12(2007), No. 2, p. 129.

[35] E. Yilmaz, *Investigating the Hydro-geotechnical and Microstructural Properties of Cemented Paste Backfills Using the Versatile Cuaps Apparatus* [Dissertation], Université du Québec en Abitibi-Témiscamingue (UQAT), Quebec City, 2010, p. 1.

[36] L. Dong, Q. Gao, S.Q. Nan, and J.Q. Du, Performance and hydration mechanism of new super fine cemented whole-tailings backfilling materials, *J. Cent. South Univ. Sci. Technol.*, 44(2013), No. 4, p. 1571.

[37] J. Dai, *Dynamic Behaviors and Blasting Theory of Rock*, Metallurgical Industry Press, Beijing, 2002, p. 60.

[38] J.X. Fu, C.F. Du, and W.D. Song, Strength sensitivity and failure mechanism of full tailings cemented backfills, *J. Univ. Sci. Technol. Beijing*, 36(2014), No. 9, p. 1149.

[39] Z.X. Liu and X.B. Li, Research on stability of high-level

backfill in blasting, *Min. Metall. Eng.* 24(2004), No. 3, p. 21.

[40] N. Li, K.P. Zhou, D. Pan, and H.L. Zhu, Study on intensity response of rubble backfill to dynamic loading of medium-length hole blasting, *Min. Metall. Eng.*, 31(2011), No. 4, p. 9.

[41] Q.L. Zhang, W. Yang, S. Yang, and M.X. Wang, Test research on stability of high-density total tailing cemented backfilling under dynamic loading, *China Saf. Sci. J.*, 25(2015), No. 3, p. 78.

[42] J.H. Sun, Y.M. Dou, J. Zhou, and B. Li, Experimental study of the effect of strain rate on compressive property of concrete, *China Concr. Cem. Prod.*, 2011, No. 5, p. 1.

[43] R.J. Chen, H.W. Liu, and R. Zeng, SHPB dynamic experiment on silica fume concrete, *Adv. Mater. Res.*, 631(2013), p. 771.

[44] C.E. Fairhurst and J.A. Hudson, Draft ISRM suggested method for the complete stress-strain curve for intact rock in uniaxial compression, *Int. J. Rock Mech. Min. Sci.*, 36(1999), No. 3, p. 279.

[45] J.Y. Xu, J.S. Fan, and X.C. Lu, *Dynamic Mechanical Properties of Rock under Confining Pressure*, Northwestern Polytechnical University Press, Xi'an, 2012, p. 56.

[46] S.S. Wang, M.H. Zhang, and S.T. Quest, Effect of sample size on static strength and dynamic increase factor of high-strength concrete from SHPB test, *J. Test. Eval.*, 39(2011), No. 5, p. 898.

[47] J.Z. Liu, J.Y. Xu, X.C Lu, L. Zhang, and Z.D. Wang, Experimental study on dynamic mechanical properties of amphibolies under impact compressive loading, *Chin. J. Rock Mech. Eng.*, 28(2009), No. 10, p. 2113.